Measured Constraints on Cloud-Top Entrainment to Reduce Uncertainty of Non-Precipitating Stratocumulus Shortwave Radiative Forcing in the Southern Ocean

Kevin Sanchez[1], Greg Roberts[2], Lynn M Russell[3], and Minghui Diao[4]

[1]Scripps Institution of Oceanography
[2]Centre National de la Recherche Scientifique
[3]University of California, San Diego
[4]San Jose State University

November 22, 2022

Abstract

Stratocumulus cloud-top entrainment has a significant effect on cloud properties, but there are few observations quantifying its impact. Using explicit 0D parcel model simulations, initialized with below-cloud in-situ measurements, and validated with in-situ measurements of cloud properties, the shortwave cloud radiative forcing (SWCF) was reduced by up to 100 W m^{-2} by cloud-top entrainment in the Southern Ocean. The impact of entrainment-corrected SWCF is between 2 and 20 times that of changes in the aerosol particle concentration or updraft at cloud base. The variability in entrainment-corrected SWCF accounts for up to 50 W m^{-2} uncertainty in estimating cloud forcing. Measurements necessary for estimating the impact of entrainment on cloud properties can be constrained from existing airborne platforms and provide a first-order approximation for cloud radiative properties of non-precipitating stratocumulus clouds. These measurement-derived estimates of entrainment can be used to validate and improve parameterizations of entrainment in Global Climate Models.

Hosted file

`supporting-information.docx` available at https://authorea.com/users/540355/articles/600195-measured-constraints-on-cloud-top-entrainment-to-reduce-uncertainty-of-non-precipitating-stratocumulus-shortwave-radiative-forcing-in-the-southern-ocean
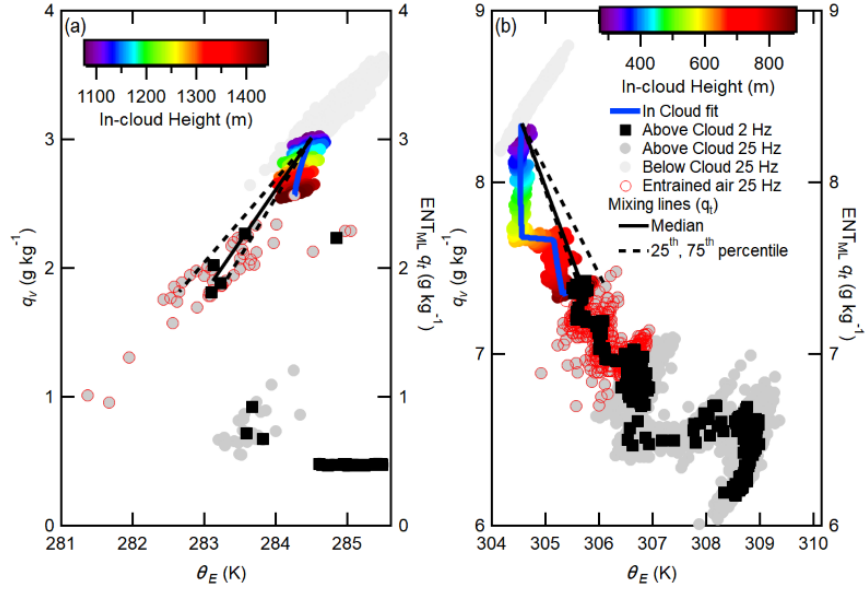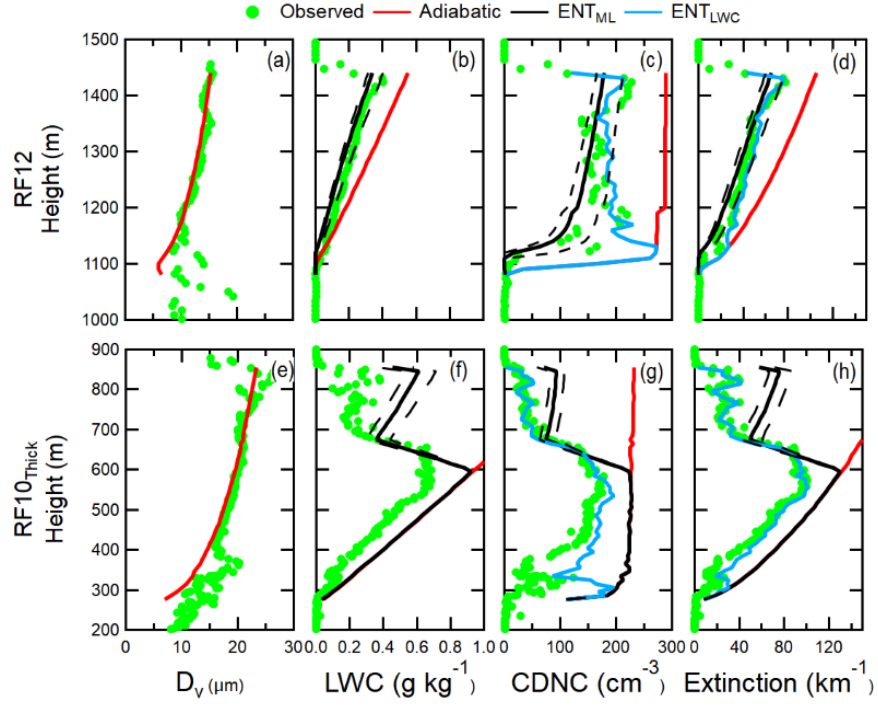
1 **Measured Constraints on Cloud-Top Entrainment to Reduce Uncertainty**

2 **of Non-Precipitating Stratocumulus Shortwave Radiative Forcing in the**

3 **Southern Ocean**

4 **K. J. Sanchez[1*], G. C. Roberts[1,2], M. Diao[3], and L. M. Russell[1]**

5 [1]Scripps Institution of Oceanography, University of California, San Diego, CA, USA
6 [2]Centre National de Recherches Météorologiques, Météo-France & CNRS UMR3589, Toulouse,
7 France
8 [3]Department of Meteorology and Climate Science, San Jose State University, San Jose, CA,
9 USA

10 Corresponding author: Kevin Sanchez (kjsanche@ucsd.edu)
11

12 *Now at: Universities Space Research Association, Columbia, MD, USA
13 Now at: NASA Langley Research Center, Hampton, VA, USA

14 **Key Points:**

15 • Basic vertical profile measurements are sufficient to constrain entrainment in non-
16 precipitating Southern Ocean (SO) stratocumulus clouds

17 • The sensitivity of shortwave cloud forcing to entrainment is 2-20 times the sensitivity to
18 particle concentration or cloud-base updraft

19 • Quantifying the impact of entrainment on shortwave cloud forcing is needed to determine
20 the energy budget in the SO

21 **Abstract**

22 Stratocumulus cloud-top entrainment has a significant effect on cloud properties, but there are
23 few observations quantifying its impact. Using explicit 0D parcel model simulations, initialized with
24 below-cloud in-situ measurements, and validated with in-situ measurements of cloud properties, the
25 shortwave cloud radiative forcing (SWCF) was reduced by up to 100 W m^{-2} by cloud-top entrainment in
26 the Southern Ocean. The impact of entrainment-corrected SWCF is between 2 and 20 times that of
27 changes in the aerosol particle concentration or updraft at cloud base. The variability in entrainment-
28 corrected SWCF accounts for up to 50 W m^{-2} uncertainty in estimating cloud forcing. Measurements
29 necessary for estimating the impact of entrainment on cloud properties can be constrained from existing
30 airborne platforms and provide a first-order approximation for cloud radiative properties of non-
31 precipitating stratocumulus clouds. These measurement-derived estimates of entrainment can be used to
32 validate and improve parameterizations of entrainment in Global Climate Models.

33

34

Plain Language Summary

Clouds over the ocean have a significant impact on climate because they reflect sun light that would otherwise be absorbed by the ocean. Understanding and accurately modeling how much sunlight these clouds reflect is important to understand feedbacks between clouds and climate. Using a simple model and cloud measurements, mixing of moist cloud air with warm-dry air from above the cloud was shown to decrease the cloud droplet number concentration and consequently total liquid water, which significantly decreases the overall amount of sunlight reflected by the cloud. Cloud droplets form onto small particles as they enter the base of the cloud through an updraft, in the meantime, warm-dry air from above the cloud mixes downward. In this study, the warm-dry air from above the cloud was shown to be more influential on reflecting sunlight than the concentration of particles and the updraft velocity at cloud-base. These results emphasize the importance of accurately accounting for the mixing in of warm-dry air from above the cloud in climate models, and can be constrained by existing measurements that are readily available on weather balloons and aircraft.

1 Introduction

Low clouds in the Southern Ocean (SO) are poorly simulated by general circulation models (GCMs) and tend to overestimate the amount of radiation absorbed by the SO (Bodas-Salcedo et al., 2014; Haynes et al., 2011; Hyder et al., 2018; McCoy et al., 2014). This bias is driven by underestimates of cloud radiative forcing, which are likely due to errors in cloud microphysical properties such as droplet size and concentration, as well as cloud processes such as precipitation and entrainment (Mason et al., 2015; Vial et al., 2013). Cloud properties in the SO are also particularly sensitive to aerosol loading due to relatively low background aerosol concentrations (Downey et al., 1990; Whittlestone & Zahorowski, 1998). Therefore, addressing these uncertainties is necessary for assessing future climate change feedbacks. GCM shortcomings, biases in satellite retrievals, and the scarcity of SO cloud measurements (Lenschow et al., 1999; Russell et al., 1998; Seinfeld et al., 2016) motivated the Southern Ocean Clouds, Radiation, Aerosol Transport Experimental Study (SOCRATES), which conducted in-situ airborne measurements of clouds, aerosol, and meteorological state over the SO on the NSF/NCAR HIAPER Gulfstream V (GV) (Laursen et al., 2006). The analysis shown here aims to improve GCM estimates of reflected shortwave radiation and the earth's energy budget by

64   obtaining measurements of cloud top entrainment drying with widely used measurements to

65   improve the parameterization of clouds in models.

66   Aerosol-cloud interactions account for a significant part of the uncertainty in the global

67   energy budget (IPCC, 2014; Lohmann, 2017; Nazarenko et al., 2017; Seinfeld et al., 2016;

68   Stevens, 2015). Variability in reflected shortwave radiation (or albedo) is caused by differences

69   in cloud fraction, cloud optical thickness, cloud droplet number concentration (CDNC) and cloud

70   lifetime (Albrecht, 1989; Jiang et al., 2006; M. Wang et al., 2012). Aerosol indirect effects such

71   as enhancements in particle concentrations leading to increased CDNC and increased reflected

72   solar radiation are classic examples of how changes in particle concentrations alter cloud optical

73   properties (Ackerman et al., 2000; Albrecht, 1989; Jiang et al., 2006; Lu & Seinfeld, 2005;

74   Twomey, 1977; Xue & Feingold, 2006). While correctly representing CDNC is a concern in

75   GCMs for accurately modeling the optical thickness of clouds, uncertainty in liquid water path

76   (LWP) accounts for more than a factor of two change in cloud optical thickness compared to

77   CDNC (Brenguier et al., 2011), making LWP of first-order importance (Boers & Ross, 1994; Lu

78   et al., 2008). One of the biggest factors in determining marine stratocumulus LWP is the cloud-

79   top entrainment rate, however, numerous feedbacks between the cloud properties and

80   entrainment make simulating and parameterizing entrainment rates challenging (Chen et al.,

81   2011). Even though cloud-top entrainment and detrainment play an important role in the

82   resulting cloud optical properties, their roles in determining cloud optical properties are not often

83   considered in aerosol-cloud closure studies.

84   Entrainment of free tropospheric air at cloud top typically results in a warmer, drier

85   boundary layer, as well as, clouds with subadiabatic LWP and decreased precipitation

86   (Ackerman et al., 2009; Chen et al., 2011; Deardorff, 1980; Hill et al., 2009; Lu & Seinfeld,

87   2005; Wood, 2007; Xue & Feingold, 2006). Under certain thermodynamic conditions, when the

88   above-cloud entrained air is excessively dry, the air mixture can result in a parcel becoming

89   negatively buoyant due to evaporative cooling, leading to enhancements in the entrainment rate

90   (Ackerman et al., 2004; Burnet & Brenguier, 2007; Grabowski, 1993). The exchange of air

91   between cloud top and the overlying air is determined by the gradient in specific humidity and

92   temperature across the inversion (Sanchez et al., 2017; Stevens, 2002), both of which are

93   expected to change in a warming climate (Qu et al., 2015). Increased temperature gradients

94   between the marine boundary layer (MBL) and free troposphere, result in stronger inversions

95   which decrease cloud-top entrainment rates (Ackerman et al., 2004; Caldwell & Bretherton,
96   2009) and increase cloud fraction (Caldwell et al., 2013). However, enhanced specific humidity
97   gradients across the inversion (Webb & Lock, 2013) also lead to increased evaporation-driven
98   entrainment at cloud-top, which thins stratocumulus clouds in LES simulations (Bretherton,
99   2015; Bretherton et al., 2013).

100   Cloud top entrainment is also affected by an aerosol-driven feedback on the entrainment
101   rate. For example, a decrease in aerosol loading leads to larger cloud droplets and an
102   enhancement in droplet sedimentation and precipitation at cloud top, which results in a decrease
103   in cloud-top LWC, and consequently, a decrease in evaporative cooling and entrainment as well
104   (Bretherton, 2015; Bretherton et al., 2007; Turton & Nicholls, 1987; Zuidema et al., 2008). Large
105   Eddy Simulation (LES) by Zuidema (2008) show increased particle concentrations are linked to
106   decreased cloud fraction as a result of more entrainment in spite of less drizzle. Further
107   complicating this process, cloud-top entrainment is initiated by mixing on centimeter to meter
108   length scales, meaning it cannot be explicitly resolved in LES models or GCMs, requiring
109   entrainment to be a parameterized process. In previous LES studies of stratocumulus clouds, the
110   vertical resolution has been increased in an attempt to reduce the uncertainty in the entrainment
111   rate and resulted in a decrease in the over-prediction of cloud-top entrainment, and consequently,
112   under-predicting the cloud radiative forcing (Bretherton et al., 1999; Stevens et al., 2005). In
113   addition, Stevens et al., (2005) found that increasing the horizontal resolution is important for
114   resolving the strength of large eddies (> 70 m), and hence, improves the calculation of the
115   entrainment rate.

116   In GCMs, the Cloud Layers Unified by Binormals (CLUBB) parameterization is the most
117   promising method of reproducing sub-grid-scale cloud properties and involves using probability
118   distribution functions (PDF) derived from sub-grid scale predictive moments to derive cloud
119   properties over multiple regimes (Guo et al., 2010, 2014). GCMs are constrained with satellite
120   measurements; however, current satellite-derived cloud properties assume a 30% reduction in
121   CDNC due to inhomogeneous entrainment (Rosenfeld et al., 2016). Entrainment drying in the
122   CLUBB parameterization can be tuned, and the mixing line approach from this study can be
123   utilized to obtain datasets for improving entrainment in the CLUBB parameterization (Guo et al.,
124   2014).

125   In this manuscript, five case studies are used to quantify the impact of cloud-top

126   entrainment on stratocumulus cloud optical properties in the SO using a concept first described

127   by Betts (1983) and Paluch (1979). Betts (1983) showed that stratocumulus clouds largely follow

128   a mixing line structure from cloud-base to cloud-top, where conservative variables are linearly

129   related, indicating that entrained air at cloud-top vertically mixes throughout the cloud. This

130   concept was recently utilized by Sanchez et al. (2017) and Calmer et al. (2019) to account for

131   entrainment-induced evaporation of cloud droplets which improved representation of non-

132   precipitating stratocumulus cloud optical properties. The method used in a pristine mid-latitude

133   marine environment (Sanchez et al., 2017) and a polluted Mediterranean region (Calmer et al.,

134   2019) is also verified for SO clouds during the SOCRATES experiment. By combining in-situ

135   measurements of cloud condensation nuclei (CCN) spectra at cloud base, vertical profiles of the

136   thermodynamic properties throughout the marine boundary layer, updraft and an aerosol-cloud-

137   parcel model (ACPM), this study obtains accurate simulations of the observed cloud optical

138   properties by incorporating the impact of entrainment on the microphysical properties of

139   stratocumulus clouds in the SO. We also relate the sensitivity of stratocumulus shortwave cloud

140   forcing (SWCF) to changes in below-cloud aerosol concentrations and updraft, as well as to the

141   impact of entrainment (ENT_{LWC}, Sections 2.4) via the reduction of liquid water path (LWP). The

142   mixing-line entrainment approximation ($ENT_{ML,}$ Sections 2.5 and 3.2) enables the calculation of

143   the entrained fraction of air and resulting sub-adiabatic LWC throughout the cloud using only

144   vertical profiles of temperature, pressure and relative humidity measurements. This technique to

145   account for entrainment can eventually be applied globally to non-precipitating stratocumulus

146   clouds using relatively simple observations to constrain and evaluate GCM parameterizations.

147   **2 Methods**

148   2.1 NSF/NCAR HIAPER GV measurements

149   Measurements used in SOCRATES are collected on the NSF/NCAR Gulfstream-V High-

150   performance Instrumented Airborne Platform for Environmental Research (GV HIAPER)

151   observational platform. The GV was stationed at the Hobart International Airport, Tasmania,

152   during the austral summer between 15 January and 24 February 2018. The flight strategy during

153   SOCRATES involved ferrying out to an area of interest followed by a series of straight vertical

154   profiles, and level legs to sample below, in and above cloud in the marine boundary layer. The

155 GV conducted 15 research flights (RF) over the SO between 42.5 °S and 62.1 °S and between

156 133.8 °E and 163.1 °E at altitudes ranging from 50-7500 m.

157   A wing-mounted Ultra-High Sensitivity Aerosol Spectrometer (UHSAS, DMT, Boulder,

158 CO) measured particle size distribution between 0.06 and 1.0 μm in diameter; however the 0.6-

159 0.7 μm bins were not used due to instrument noise at these sizes. A condensation particle counter

160 (CPC, TSI 3760A) was used to measure total particle concentrations (N_p, diameter > 10 nm).

161 CCN measurements were performed with two miniature continuous-flow stream-wise thermal

162 gradient chambers, one in scanning supersaturation mode and one in constant supersaturation

163 mode (Roberts & Nenes, 2005). The supersaturation range in the scanning CCN counter spanned

164 from 0.06-0.87 % and a single spectrum recorded every five minutes. The constant

165 supersaturation CCN counter operated at 0.43 % supersaturation, at 1 Hz. The internal chamber

166 pressure of both CCN counters was controlled to 400 hPa. Updraft distributions at cloud base

167 were measured by the GV HIAPER Cloud Radar (HCR), corrected for plane orientation with

168 nadir looking data. HCR reflectance and a Particle Habit Imaging and Polar Scattering probe

169 (Abdelmonem et al., 2016; Schnaiter et al., 2018) were also used to identify clouds without

170 drizzle (Chin et al., 2000; Kato et al., 2001; Kogan et al., 2005). A high frequency (25 Hz)

171 Vertical Cavity Surface Emitting Laser (VCSEL) water vapor hydrometer was used to measure

172 the water vapor mixing ratio (Zondlo et al., 2010). A QA/QC water vapor dataset at 25 Hz for

173 the SOCRATES campaign (Diao, 2020) is further used to derive specific humidity (q_v) and

174 relative humidity with respect to liquid (RH_{liq}). Finally, a cloud droplet probe (CDP, DMT,

175 Boulder, CO) is used to measure cloud droplet concentration and size (2-50 μm diameter) to

176 calculate liquid water content (LWC) and cloud droplet extinction for comparison with the

177 ACPM (section 2.2).

178   2.2 Aerosol Cloud Parcel Model (ACPM) description

179   A 0D ACPM was used in this study because 1) it enables the simulated results to be

180 constrained by measured thermodynamic properties, aerosol number size distributions, and CCN

181 spectra (Table 1, Supporting Figure S1); and 2) the ACPM allows explicit comparison to in-situ

182 measurements of cloud droplet size distributions (rather than parameterized cloud droplet size

183 distributions used in LES). The ACPM is based on a fixed-sectional approach to represent the

184 dry particle size domain, with internally-mixed chemical components. The model employs a

185   dual-moment (number and mass) algorithm (Tzivion et al., 1987) to calculate particle growth

186   from one size section to the next for non-evaporating compounds (namely, all components other

187   than water) using an accommodation coefficient of 1.0 (Raatikainen et al., 2013). Liquid water is

188   treated in a moving-section representation, similar to the approach of Jacobson et al. (1994), to

189   account for evaporation and condensation of water in conditions of varying humidity. The model

190   includes a dynamic scheme for activation of particles to cloud droplets (Seinfeld & Pandis,

191   2006). Aerosol hygroscopicity was calculated using the UHSAS particle size distribution, CCN

192   spectra and κ-Köhler theory (Kohler, 1936; Petters & Kreidenweis, 2007) in below-cloud

193   samples by matching cumulative UHSAS distributions with CCN concentrations at all sizes

194   above 70 nm diameter. The hygroscopicity of particles below 70 nm was considered to be the

195   same as the calculated hygroscopicity at 70 nm. The CPC concentration and cumulative particle

196   number distribution from the UHSAS were used to linearly interpolate particle concentrations

197   between 10 and 70 nm diameter. In subsaturated conditions (i.e., relatively humidity < 100%),

198   aerosol particles below the cloud base are considered to be in local equilibrium with water vapor

199   pressure. A detailed description of the Aerosol Cloud Parcel Model (ACPM) is presented in

200   Russell and Seinfeld (1998) and Russell et al. (1999). The criteria for selecting case studies is

201   discussed in Supporting text S1.

202   The ACPM in-cloud lapse rate is adiabatic, and ultimately compared to observations to

203   assess entrainment (Sections 2.4 and 2.5). A weighted ensemble of positive vertical velocities

204   (Supporting Figure S1a) measured with the NCAR/NSF GV HIAPER cloud radar were applied

205   to the ACPM to produce the simulated cloud droplet distribution (Sanchez et al., 2016). The

206   shortwave cloud forcing (SWCF) is calculated as $SWCF = \alpha Q$, where Q is the day average solar

207   insolation (Table 1) based on the latitude and α is the cloud albedo which is derived from the

208   vertical profile of the in-situ (CDP) and simulated (ACPM) cloud droplet size distribution and an

209   asymmetric scattering parameter of 0.85 (see Supporting text S2) (Bohren & Battan, 1980;

210   Geresdi et al., 2006; Hansen & Travis, 1974; Sanchez et al., 2017; Stephens, 1978). Coagulation,

211   scavenging, and deposition of the aerosol were included in the ACPM, but their effects are

212   negligible given the relatively short simulations used here (< 1 h), and their relatively low marine

213   total aerosol particle concentrations (< 1000 cm^{-3}) and cloud LWC (< 1 g m^{-3}). As stated

214   previously, cloud droplet sizes were < 20 μm diameter (for all but one case (RF10$_{Thick}$; Table 1),

215 therefore, autoconversion and accretion rates are not included in this simulation and exert a

216 negligible effect on the simulated values of LWC and CDNC (Feingold et al., 2013).

217   2.3 ACPM cloud-top entrainment

218   The process of entrainment and its effect on a cloud can be described as the weighted

219 downward mixing of above-cloud warm, dry air into the cloudy air below causing cloud droplets

220 to evaporate. This air-parcel, subsequently mixes downward, diluting the cloud droplet

221 concentration throughout the cloud, resulting in a reduction in CDNC compared to an adiabatic

222 profile (Chen et al., 2011; S. Wang et al., 2003; Xue & Feingold, 2006). Five cases are available

223 from this campaign to illustrate the effect of entrainment on SWCF in the SO (Table 1). These

224 five cases are from four different research flights (RF) and are referred to by their flight number,

225 with the two RF10 cases being differentiated by subscripts that describe the cloud thickness

226 ($RF10_{Thin}$ or $RF10_{Thick}$). Simulated cloud profiles are produced using the ACPM using adiabatic

227 conditions, which are then compared to in-situ observations and corrected for cloud-top

228 entrainment.

229   2.4 Entrainment Derived from Liquid Water Content (ENT_{LWC})

230   The relative difference between simulated and observed values of LWC (or LWP) is

231 related to the entrained fraction of above-cloud air. To account for the decrease in LWC

232 associated with entrainment, the CDNC in the ACPM is decreased until the simulated (ACPM)

233 and observed (CDP) LWC vertical profiles are the same. This approximation assumes

234 inhomogeneous mixing, meaning only a fraction of the cloud droplets evaporate, whereas

235 homogenous mixing implies all cloud droplets partially evaporate. Inhomogeneous mixing is

236 consistent with past studies of well-mixed, non-precipitating stratocumulus clouds (Brenguier et

237 al., 2011; Burnet & Brenguier, 2007; Jia et al., 2019). Furthermore, homogeneous mixing would

238 not sufficiently account for the observed decrease in SWCF and CDNC. In this study,

239 evaporation of droplets due to inhomogeneous mixing is independent of droplet size, therefore

240 the volumetric mean diameter does not change due to droplet evaporation.

241   2.5 Entrainment Derived from a Mixing Line (ENT_{ML})

242   ENT_{ML} accounts for the sub-adiabatic LWC values due to cloud-top entrainment with

243 inhomogeneous mixing, derived from temperature, pressure and q_v measurements. ENT_{ML}, first

244 used by Sanchez et al. (2017) and Calmer et al. (2019), generates a mixing line (a linear

245   relationship between two conservative variables, Figure 1) between q_v at the cloud-base and

246   above-cloud, and measurement-derived equivalent potential temperature (θ_E). q_v is equivalent to

247   total water content (q_t), a conservative variable, in these subsaturated, non-precipitating

248   conditions. With the mixing line, the in-cloud q_t is a function of θ_E, which is derived from in-

249   cloud temperature, pressure and q_v (See Supporting text S3, Figure S3). The measured

250   thermodynamic properties of the above-cloud air (shown as red squares in Figure 1) and cloud-

251   base air are then used to estimate subadiabatic LWC profile (Calmer et al., 2019; Sanchez et al.,

252   2017). In this analysis, a line is made between a point at the cloud base and each point above the

253   cloud that is identified as 'entrained air' (red-bounded grey markers in Figure 1 and

254   Supplemental Figure S4). Each line is used to calculate an entrainment-corrected vertical profile

255   of CDNC, LWC, cloud droplet extinction and integrated SWCF. The solid black line in Figure 1

256   and 2 is the 50th percentile (median) of the CDNC, LWC and extinction, while the black dashed

257   lines represent the 25th and 75th percentiles. See the Supporting text S3 and S4 for details on the

258   measurements that represent the entrained air that are used to derive sub-adiabatic cloud liquid

259   water content.

3 Results

261   The observed LWC profiles in the SO are sub-adiabatic (Figure 2b,f) for all cases studied

262   during the SOCRATES experiment. CDNCs are also always lower than the adiabatic simulations

263   (Table 1, Figure 2) while the volumetric diameter (D_v) is consistent with adiabatic simulations,

264   suggesting entrainment of dry air is reducing LWC via the evaporation of cloud droplets. These

265   results are consistent with previous observations in the SO (Yum et al., 1998), the tropics

266   (Rauber et al., 2007; Roberts et al., 2008) and mid-latitudes (Calmer et al., 2019; Sanchez et al.,

267   2017). Consequently, the SWCF and CDNCs above cloud-base are significantly and consistently

268   overestimated compared to adiabatic conditions (Table 1).

269   3.1 ENT$_{LWC}$; comparison of ACPM to observations

270   To illustrate the impact of entrainment on cloud microphysical and optical properties,

271   Figure 2 shows the vertical profiles of observed and simulated D_v, LWC, CDNC, and cloud

272   droplet extinction for RF12 and RF10$_{Thick}$ to illustrate two distinctly different cases for which

273   entrainment corrections may be applied. The adiabatic ACPM overestimates the observed LWC,

274   CDNC, and cloud droplet extinction; however, D_v remains remarkably similar to observed

275   values, which supports evidence for inhomogeneous mixing (Brenguier et al., 2011; Burnet &

276   Brenguier, 2007; Jia et al., 2019).

277   In-cloud level-legs that straddled the vertical profiles for RF02 and RF13 cases, shown in

278   Supporting Figure S6 show LWC, CDNC, and D_v varied consistently together over tens of

279   kilometers, suggesting that inhomogeneous mixing also remains consistent over tens of

280   kilometers. The horizontal variability in-cloud properties corresponds to changes in the cloud

281   base height, as shown by the downward facing HIAPER radar reflectivity during the RF13 in-

282   cloud level-leg (Supporting Figure S7). By accounting for entrainment with ENT_{LWC} (Section

283   2.4), simulated CDNC and extinction reproduce observed values.

284   Table 1 shows the difference in SWCFs comparing observations to the adiabatic model

285   ($\delta SWCF_{adiabatic}$) and accounting for entrainment using LWC ($\delta SWCF_{ENT_{LWC}}$) and mixing line

286   ($\delta SWCF_{ENT_{ML}}$) corrections. A difference of 0 W m^{-2} implies adiabaticity. $\delta SWCF_{adiabatic}$

287   represents the upper limit and ranged from 38.4±8.9 to 93.4±17.1 W m^{-2}; while

288    $\delta SWCF_{ENT_{LWC}}$ are significantly lower, between 5.3±16.2 and 32.1±14.2 W m^{-2}. As LWC in the

289   observed and ENT_{LWC} vertical profiles are, by definition, the same, $\delta SWCF_{ENT_{LWC}}$ is greater than

290   zero because of narrower droplet spectrum width and greater CDNC in the simulations.

291   Compared to the adiabatic simulations, CDP-derived LWP was reduced by 28%-58% as a result

292   of cloud-top entrainment. For these five cases, the range in SWCF associated with 28% and 58%

293   reduction in LWP compared to an adiabatic LWP amounts to 53 W m^{-2} (Table 1). This implies

294   that variability in entrainment exerts an uncertainty in radiative forcing of individual clouds up to

295   50 W m^{-2}.

296   The ACPM was used to further quantify and compare the sensitivity of SWCF and

297   CDNC to changes in aerosol (N_p), updraft (w), and LWP related to entrainment (Table 1). In

298   these sensitivity calculations, N_p and *w* distributions were evaluated at half and double their

299   observed values (i.e., 0.5N_p and 2N_p; 0.5*w* and 2*w*). Table 1 shows that SWCF is 2-4 times more

300   sensitivity to N_p than *w* over the SO. Similarly, CDNC was approximately 1-3 times more

301   sensitive to N_p than *w*. This indicates that clouds in the SO form in an aerosol-limited regime,

302   which is characteristic of the marine boundary layer (Reutter et al., 2009; Sanchez et al., 2016).

303   Table 1 shows that the SWCF sensitivity to entrainment and subsequent reduction of LWP are 2-

304   20 times those related to N_p and w. CDNC is approximately twice as sensitive to entrainment

305   compared to N_p and up to four times more sensitive than the updraft. This highlights the first-

306   order role of entrainment in determining cloud microphysical properties.

307   The SWCF for RF02 and RF10$_{thick}$ illustrate limiting cases in this study as they are the

308   most and least sensitive, respectively, to both N_p and entrainment. The RF02 SWCF case shows

309   the greatest sensitivity to N_p and entrainment because it has the lowest CDNC concentration and

310   it is the thinnest cloud of the five cases ($\delta SWCF_{ENT_{LWC}}$ = 32.1±14.2 W m^{-2}; Table 1). In contrast,

311   the impact of entrainment on RF10$_{Thick}$ is lower than the other cases in this study because the

312   cloud is significantly thicker (Table 1), and the cloud SWCF is less sensitive to changes in

313   optical thickness when the optical thickness is high (Sanchez et al., 2016) (Supporting Figure

314   S8). The RF10$_{Thick}$ case is also unique relative to the other cases because it has a large Aitken

315   mode, as well as the highest CCN concentration (Supporting Figure S1c, Table 1). The RF10$_{Thick}$

316   CDNC is more sensitive to N_p than *w* (aerosol-limited case; Reutter et al., 2009); however, it is

317   relatively more sensitive to *w* compared to the other cases in this study because of the high

318   Aitken mode particle concentration (similar to findings by Sanchez et al. (2016)).

319   3.2 ENT$_{ML}$; comparison of ACPM to observations

320   Compensating SWCF for entrainment mixing using ENT$_{ML}$ (Section 2.5) and ENT$_{LWC}$

321   (Section 2.4) yield similar results (within ~ 15 W m^{-2}) for three out of the five cases of

322   observations (Table 1). For RF10, compensating SWCF using ENT$_{ML}$ yielded results within ~50

323   W m^{-2} (RF10$_{Thin}$ ($\delta SWCF_{ENT_{ML}}$ = 54.2±16.2 W m^{-2}); RF10$_{Thick}$ ($\delta SWCF_{ENT_{ML}}$ = 27.6±12.8 W m^{-2};

324   Table 1), showing only a relatively small improvement compared to $\delta SWCF_{adiabatic}$. The main

325   limitation of ENT$_{ML}$ results from discrepancies in the approximation of LWC (and LWP), as

326   ENT$_{ML}$ utilizes a linear relationship of q_t and θ_E (conservative variables) between the top and

327   bottom of the cloud to calculate q_t as a function of the measurement-derived θ_E in the cloud.

328   Since θ_E is a function of q_v and temperature, these two variables may co-vary, yet θ_E remains

329   constant even while q_t may vary vertically in the cloud. In such a case, the ENT$_{ML}$-derived q_t

330   would also be constant and represents an adiabatic limit. For example, RF10$_{Thick}$ shows a

331   constant θ_E between cloud base (290 m) and ~600 m, which is also the same altitude as an in-

332   cloud temperature inversion (Figure 1b, Supporting Figure S3d,i). As θ_E is constant, ENT$_{ML}$-

333   derived q_t approaches the adiabatic limit even though the observed values of q_t decrease ~0.2 g

334   kg^{-1} in this section of the cloud based on CDP observations (not shown). RF10$_{Thin}$ (Supporting

335 Figures S3 and S4) also has a nearly constant in-cloud θ_E, resulting in an overestimation of q_t

336 (and LWP).

337   In summary, a constant in-cloud θ_E yields ENT_{ML}-derived q_t profiles that approach

338 adiabatic LWP, CDNC and SWCF limits. Consequently, ENT_{ML} represents a minimum limit (but

339 still substantial improvement) for assessing the impact of entrainment on non-precipitating cloud

340 microphysical and radiative properties.

341 **4 Discussion and Implications**

342   This study uses in-situ measurements from the Southern Ocean Clouds, Radiation,

343 Aerosol Transport Experimental Study (SOCRATES), collected on the NSF/NCAR HIAPER

344 Gulfstream V (GV) during the austral summer. Measurements were used to assess the impact of

345 cloud-top entrainment by combining in-situ observations of cloud condensation nuclei (CCN)

346 spectra, aerosol number size distributions and updrafts at cloud base to initialize an aerosol-cloud

347 parcel model (ACPM) and compare simulated cloud microphysical and optical properties to

348 those derived by a cloud droplet probe (CDP). Differences in shortwave cloud forcing (SWCF)

349 between adiabatic simulations and subadiabatic observations of a non-precipitating

350 stratocumulus cloud layer in the SO resulted in values as high as ~100 W m^{-2}. SWCF was

351 simulated to within 16 W m^{-2} using CDP-derived entrainment (ENT_{LWC}) for four of the five

352 cases. In one of the cases (RF02), the difference between ENT_{LWC} and observed SWCF is

353 relatively large due to the higher sensitivity of SWCF to particle concentrations. This case was

354 also the thinnest cloud in this study, and SWCF sensitivity to entrainment is higher for such

355 conditions (Supporting Figure S8).

356   Even when accounting for the impacts of entrainment on cloud optical properties, the

357 entrainment-corrected LWP varied between 28%-58%, which translates to a range of 53 W m^{-2}

358 in SWCF related to variability in entrainment for the cases studied here. For comparison, the

359 sensitivity of SWCF due to entrainment is between 2 and 20 times the sensitivities of SWCF

360 related to particle concentration and updraft – thus emphasizing the importance of accurately

361 accounting for entrainment in climate models.

362   ENT_{ML} (mixing-line approach) was simulated to within 15 W m^{-2} except for two cases.

363 ENT_{ML} utilizes the linear relationship of two conservative variables (total water content (q_t) and

364 θ_E) to derive in-cloud q_t from the measured in-cloud θ_E to calculate the entrainment-induced

365 reduction in LWP. This method was first shown in pristine and polluted mid-latitude clouds
366 (Calmer et al., 2019; Sanchez et al., 2017), and is now reproduced here with in-situ CDP
367 measurements for clouds in the SO. ENT_{ML} only requires measurements of pressure,
368 temperature, and relative humidity (PTU) in and above the cloud as well as the vertical extent of
369 the cloud to estimate the sub-adiabatic LWC profile. ENT_{LWC} is certainly a more accurate
370 method to account for entrainment, but also requires the deployment of a CDP (or similar
371 instrument to measure CDNC and LWC), which is not nearly as ubiquitous as PTU
372 measurements. PTU measurements can be obtained with numerous airborne platforms (i.e.,
373 radiosondes, aircraft and UAVs) as long as the vertical resolution is high enough to capture the
374 temperature and water vapor immediately above the cloud layer (within ~10 to 100 meters).

375 ENT_{ML} approaches an adiabatic profile (i.e., no entrainment correction), if θ_E remains
376 constant in the cloud while q_t actually varies. Nonetheless, ENT_{ML} could be used to improve
377 GCM parameterizations, such as multivariate PDFs representing sub-grid-scale moisture,
378 temperature and vertical velocity to derive cloud microphysical parameters across multiple cloud
379 regimes (Guo et al., 2010). Reducing the uncertainty of cloud optical properties in GCM models
380 remains a fundamental challenge for correctly representing the Earth's energy budget
381 (Bretherton et al., 2013; Brient et al., 2019; Hourdin et al., 2015; de Szoeke et al., 2010). For
382 decades now, the IPCC has reported an uncertainty in the anthropogenic-induced cloud forcing
383 of approximately 1.5 W m^{-2}, which represents nearly 75% of the uncertainty related to the total
384 anthropogenic radiative forcing (IPCC, 2014). This study in the SO extends beyond earlier
385 studies in the mid-latitudes (Sanchez et al., 2016; Calmer et al., 2019) to show that the reduction
386 in LWP owing to entrainment is a major contributor to uncertainty in SWCF for stratocumulus
387 clouds globally. Improving the parameterizations of entrainment using the mixing line
388 techniques presented here has the potential to significantly improve GCM representation of cloud
389 optical properties and, ultimately, the Earth's energy budget.

390 **Acknowledgments**

References

400

401 Abdelmonem, A., Järvinen, E., Duft, D., Hirst, E., Vogt, S., Leisner, T., & Schnaiter, M. (2016).

402 PHIPS-HALO: The airborne Particle Habit Imaging and Polar Scattering probe-Part 1:

403 Design and operation. *Atmospheric Measurement Techniques*, *9*(7), 3131–3144.

404 https://doi.org/10.5194/amt-9-3131-2016

405 Ackerman, A. S., Toon, O. B., Taylor, J. P., Johnson, D. W., Hobbs, P. V., Ferek, R. J., et al.

406 (2000). Effects of Aerosols on Cloud Albedo: Evaluation of Twomey's Parameterization of

407 Cloud Susceptibility Using Measurements of Ship Tracks. *Journal of the Atmospheric*

408 *Sciences*, *57*(16), 2684–2695. https://doi.org/10.1175/1520-

409 0469(2000)057<2684:EOAOCA>2.0.CO;2

410 Ackerman, A. S., Kirkpatrick, M. P., Stevens, D. E., & Toon, O. B. (2004). The impact of

411 humidity above stratiform clouds on indirect aerosol climate forcing. *Nature*, *432*(7020),

412 1014–1017. https://doi.org/10.1038/nature03174

413 Ackerman, A. S., vanZanten, M. C., Stevens, B., Savic-Jovcic, V., Bretherton, C. S., Chlond, A.,

414 et al. (2009). Large-Eddy Simulations of a Drizzling, Stratocumulus-Topped Marine

415 Boundary Layer. *Monthly Weather Review*, *137*(3), 1083–1110.

416 https://doi.org/10.1175/2008MWR2582.1

417 Albrecht, B. A. (1989). AEROSOLS, CLOUD MICROPHYSICS, AND FRACTIONAL

418 CLOUDINESS. *Science*, *245*(4923), 1227–1230.

419 https://doi.org/10.1126/science.245.4923.1227

420 Betts, A. K. (1983). Thermodynamics of mixed stratocumulus layers: saturation point budgets.

421 *Journal of the Atmospheric Sciences*, *40*(11), 2655–2670. https://doi.org/10.1175/1520-

422 0469(1983)040<2655:TOMSLS>2.0.CO;2

423 Bodas-Salcedo, A., Williams, K. D., Ringer, M. A., Beau, I., Cole, J. N. S., Dufresne, J.-L., et al.

424 (2014). Origins of the Solar Radiation Biases over the Southern Ocean in CFMIP2

425 Models*. *Journal of Climate*, *27*(1), 41–56. https://doi.org/10.1175/JCLI-D-13-00169.1

426 Boers, R., & Ross, M. M. (1994). Absorption feedback in stratocumulus clouds Influence on

427   cloud top albedo. *Tellus*, (0280–6495), 229–241.

428   Bohren, C. F., & Battan, L. J. (1980). Radar Backscattering by Inhomogeneous Precipitation

429   Particles. *Journal of the Atmospheric Sciences*, *37*(8), 1821–1827.

430   https://doi.org/10.1175/1520-0469(1980)037<1821:RBBIPP>2.0.CO;2

431   Brenguier, J. L., Burnet, F., & Geoffroy, O. (2011). Cloud optical thickness and liquid water

432   path-does the k coefficient vary with droplet concentration? *Atmospheric Chemistry and*

433   *Physics*, *11*(18), 9771–9786. https://doi.org/10.5194/acp-11-9771-2011

434   Bretherton, C. S. (2015). Insights into low-latitude cloud feedbacks from high-resolution models.

435   *Philosophical Transactions of the Royal Society A: Mathematical, Physical and*

436   *Engineering Sciences*, *373*(2054). https://doi.org/10.1098/rsta.2014.0415

437   Bretherton, C. S., Macvean, M. K., Bechtold, P., Chlond, A., Cotton, W. R., Cuxart, J., et al.

438   (1999). An intercomparison of radiatively driven entrainment and turbulence in a smoke

439   cloud, as simulated by different numerical models. *Quarterly Journal of the Royal*

440   *Meteorological Society*, *125*(554), 391–423. https://doi.org/10.1002/qj.49712555402

441   Bretherton, C. S., Blossey, P. N., & Uchida, J. (2007). Cloud droplet sedimentation, entrainment

442   efficiency, and subtropical stratocumulus albedo. *Geophysical Research Letters*, *34*(3),

443   L03813. https://doi.org/10.1029/2006GL027648

444   Bretherton, C. S., Blossey, P. N., & Jones, C. R. (2013). Mechanisms of marine low cloud

445   sensitivity to idealized climate perturbations: A single-LES exploration extending the

446   CGILS cases. *Journal of Advances in Modeling Earth Systems*, *5*(2), 316–337.

447   https://doi.org/10.1002/jame.20019

448   Brient, F., Roehrig, R., & Voldoire, A. (2019). Evaluating Marine Stratocumulus Clouds in the

449   CNRM-CM6-1 Model Using Short-Term Hindcasts. *Journal of Advances in Modeling*

450   *Earth Systems*, *11*(1), 127–148. https://doi.org/10.1029/2018MS001461

451   Burnet, F., & Brenguier, J. L. (2007). Observational study of the entrainment-mixing process in

452   warm convective clouds. *Journal of the Atmospheric Sciences*, *64*(6), 1995–2011.

453   https://doi.org/10.1175/JAS3928.1

454 Caldwell, P. M., & Bretherton, C. S. (2009). Response of a subtropical stratocumulus-capped

455   mixed layer to climate and aerosol changes. *Journal of Climate*, *22*(1), 20–38.

456   https://doi.org/10.1175/2008JCLI1967.1

457 Caldwell, P. M., Zhang, Y., Klein, S. A., Caldwell, P. M., Zhang, Y., & Klein, S. A. (2013).

458   CMIP3 subtropical stratocumulus cloud feedback interpreted through a mixed-layer model.

459   *Journal of Climate*, *26*(5), 1607–1625. https://doi.org/10.1175/JCLI-D-12-00188.1

460 Calmer, R., Roberts, G. C., Sanchez, K. J., Sciare, J., Sellegri, K., Picard, D., et al. (2019).

461   Aerosol Cloud Closure Study on Cloud Optical Properties using Remotely Piloted Aircraft

462   Measurements during a BACCHUS Field Campaign in Cyprus. *Atmospheric Chemistry and*

463   *Physics Discussions*, 1–35. https://doi.org/10.5194/acp-2019-8

464 Chen, Y.-C., Xue, L., Lebo, Z. J., Wang, H., Rasmussen, R. M., & Seinfeld, J. H. (2011).

465   Atmospheric Chemistry and Physics A comprehensive numerical study of aerosol-cloud-

466   precipitation interactions in marine stratocumulus. *Atmos. Chem. Phys*, *11*, 9749–9769.

467   https://doi.org/10.5194/acp-11-9749-2011

468 Chin, H. N. S., Rodriguez, D. J., Cederwall, R. T., Chuang, C. C., Grossman, A. S., Yio, J. J., et

469   al. (2000). A microphysical retrieval scheme for continental low-level stratiform clouds:

470   Impacts of the subadiabatic character on microphysical properties and radiation budgets.

471   *Monthly Weather Review*, *128*(7 II), 2511–2527. https://doi.org/10.1175/1520-

472   0493(2000)128<2511:amrsfc>2.0.co;2

473 Deardorff, J. W. (1980). Stratocumulus-capped mixed layers derived from a three-dimensional

474   model. *Boundary-Layer Meteorology*, *18*(4), 495–527. https://doi.org/10.1007/BF00119502

475 Diao, M. (2020). VCSEL 25 Hz Water Vapor Data. Version 1.0. UCAR/NCAR - Earth

476   Observing Laboratory. https://doi.org/https://doi.org/10.26023/V925-2H41-SD0F

477 Downey, A., Jasper, J. D., Gras, J. J., & Whittlestone, S. (1990). Lower tropospheric transport

478   over the Southern Ocean. *Journal of Atmospheric Chemistry*, *11*(1), 43–68.

479   https://doi.org/10.1007/BF00053667

480 Feingold, G., Eberhard, W. L., Veron, D. E., & Previdi, M. (2003). First measurements of the

481   Twomey indirect effect using ground-based remote sensors. *Geophysical Research Letters*,

482   *30*(6). https://doi.org/10.1029/2002gl016633

483   Feingold, G., McComiskey, A., Rosenfeld, D., & Sorooshian, A. (2013). On the relationship

484   between cloud contact time and precipitation susceptibility to aerosol. *Journal of*

485   *Geophysical Research-Atmospheres*, *118*(18), 10544–10554.

486   https://doi.org/10.1002/jgrd.50819

487   Geresdi, I., Meszaros, E., & Molnar, A. (2006). The effect of chemical composition and size

488   distribution of aerosol particles on droplet formation and albedo of stratocumulus clouds.

489   *Atmospheric Environment*, *40*(10), 1845–1855.

490   https://doi.org/10.1016/j.atmosenv.2005.11.012

491   Grabowski, W. W. (1993). Cumulus entrainment, fine-scale mixing, and buoyancy reversal.

492   *Quarterly Journal of the Royal Meteorological Society*, *119*(513), 935–956.

493   https://doi.org/10.1002/qj.49711951305

494   Guo, H., Golaz, J. C., Donner, L. J., Larson, V. E., Schanen, D. P., & Griffin, B. M. (2010).

495   Multi-variate probability density functions with dynamics for cloud droplet activation in

496   large-scale models: Single column tests. *Geoscientific Model Development*, *3*(2), 475–486.

497   https://doi.org/10.5194/gmd-3-475-2010

498   Guo, H., Golaz, J. C., Donner, L. J., Ginoux, P., & Hemler, R. S. (2014). Multivariate probability

499   density functions with dynamics in the GFDL atmospheric general circulation Model:

500   Global tests. *Journal of Climate*, *27*(5), 2087–2108. https://doi.org/10.1175/JCLI-D-13-

501   00347.1

502   Hansen, J. E., & Travis, L. D. (1974). Light-Scattering in Planetary Atmospheres. *Space Science*

503   *Reviews*, *16*(4), 527–610. https://doi.org/10.1007/bf00168069

504   Haynes, J. M., Jakob, C., Rossow, W. B., Tselioudis, G., Brown, J., Haynes, J. M., et al. (2011).

505   Major Characteristics of Southern Ocean Cloud Regimes and Their Effects on the Energy

506   Budget. *Journal of Climate*, *24*(19), 5061–5080. https://doi.org/10.1175/2011JCLI4052.1

507   Hill, A. A., Feingold, G., & Jiang, H. (2009). The influence of entrainment and mixing

508   assumption on aerosol-cloud interactions in marine stratocumulus. *Journal of the*

509   *Atmospheric Sciences*, *66*(5), 1450–1464. https://doi.org/10.1175/2008JAS2909.1

510   Hourdin, F., Gǝinusǝ-Bogdan, A., Braconnot, P., Dufresne, J. L., Traore, A. K., & Rio, C.

511   (2015). Air moisture control on ocean surface temperature, hidden key to the warm bias

512   enigma. *Geophysical Research Letters*, *42*(24), 10885–10893.

513   https://doi.org/10.1002/2015GL066764

514   Hyder, P., Edwards, J. M., Allan, R. P., Hewitt, H. T., Bracegirdle, T. J., Gregory, J. M., et al.

515   (2018). Critical Southern Ocean climate model biases traced to atmospheric model cloud

516   errors. *Nature Communications*, *9*(1). https://doi.org/10.1038/s41467-018-05634-2

517   IPCC. (2014). *Climate Change 2014: Impacts, Adaptation, and Vulnerability. Part A: Global*

518   *and Sectoral Aspects. Contribution of Working Group II to the Fifth Assessment Report of*

519   *the Intergovernmental Panel on Climate Change [Field, C.B., V.R. Barros, D.J. Dokken,*

520   *K.J.* Cambridge, United Kingdom and New York, NY, USA: Cambridge University Press.

521   Jacobson, M. Z., Turco, R. P., Jensen, E. J., & Toon, O. B. (1994). Modeling Coagulation

522   Among Particles of Different Composition and Size. *Atmospheric Environment*, *28*(7),

523   1327–1338. https://doi.org/10.1016/1352-2310(94)90280-1

524   Jia, H., Ma, X., & Liu, Y. (2019). Exploring aerosol cloud interaction using VOCALS-REx

525   aircraft measurements. *Atmospheric Chemistry and Physics Discussions*, *3*, 1–26.

526   https://doi.org/10.5194/acp-2018-667

527   Jiang, H., Xue, H., Teller, A., Feingold, G., & Levin, Z. (2006). Aerosol effects on the lifetime of

528   shallow cumulus. *Geophysical Research Letters*, *33*(14), 2–5.

529   https://doi.org/10.1029/2006GL026024

530   Kato, S., Mace, G. G., Clothiaux, E. E., Liljegren, J. C., & Austin, R. T. (2001). Doppler cloud

531   radar derived drop size distributions in liquid water stratus clouds. *Journal of the*

532   *Atmospheric Sciences*, *58*(19), 2895–2911. https://doi.org/10.1175/1520-

533   0469(2001)058<2895:DCRDDS>2.0.CO;2

534   Kogan, Z. N., Mechem, D. B., & Kogan, Y. L. (2005). Assessment of variability in continental

535   low stratiform clouds based on observations of radar reflectivity. *Journal of Geophysical*

536   *Research D: Atmospheres*, *110*(18), 1–15. https://doi.org/10.1029/2005JD006158

537 Kohler, H. (1936). The nucleus in and the growth of hygroscopic droplets. *Transactions of the*

538   *Faraday Society*, *32*(2), 1152–1161. https://doi.org/10.1039/tf9363201152

539 Laursen, K. K., Jorgensen, D. P., Brasseur, G. P., Ustin, S. L., & Huning, J. R. (2006). Hiaper:

540   The next generation NSF/NCAR research aircraft. *Bulletin of the American Meteorological*

541   *Society*, *87*(7), 896–909. https://doi.org/10.1175/BAMS-87-7-896

542 Lenschow, D. H., Krummel, P. B., & Siems, S. T. (1999). Measuring entrainment, divergence,

543   and vorticity on the mesoscale from aircraft. *Journal of Atmospheric and Oceanic*

544   *Technology*, *16*(10), 1384–1400. https://doi.org/10.1175/1520-

545   0426(1999)016<1384:medavo>2.0.co;2

546 Lohmann, U. (2017). Anthropogenic Aerosol Influences on Mixed-Phase Clouds. *Current*

547   *Climate Change Reports*, *3*(1), 32–44. https://doi.org/10.1007/s40641-017-0059-9

548 Lu, M. L., & Seinfeld, J. H. (2005). Study of the aerosol indirect effect by large-eddy simulation

549   of marine stratocumulus. *Journal of the Atmospheric Sciences*, *62*(11), 3909–3932.

550   https://doi.org/10.1175/JAS3584.1

551 Lu, M. L., Feingold, G., Jonsson, H. H., Chuang, P. Y., Gates, H., Flagan, R. C., & Seinfeld, J.

552   H. (2008). Aerosol-cloud relationships in continental shallow cumulus. *Journal of*

553   *Geophysical Research Atmospheres*, *113*(15), 1–21. https://doi.org/10.1029/2007JD009354

554 Martin, G. M., Johnson, D. W., & Spice, A. (1994). The Measurement and Parameterization of

555   Effective Radius of Droplets in Warm Stratocumulus Clouds. *Journal of the Atmospheric*

556   *Sciences*. https://doi.org/10.1175/1520-0469(1994)051<1823:tmapoe>2.0.co;2

557 Mason, S., Fletcher, J. K., Haynes, J. M., Franklin, C., Protat, A., Jakob, C., et al. (2015). A

558   Hybrid Cloud Regime Methodology Used to Evaluate Southern Ocean Cloud and

559   Shortwave Radiation Errors in ACCESS. *Journal of Climate*, *28*(15), 6001–6018.

560   https://doi.org/10.1175/JCLI-D-14-00846.1

561 McCoy, D. T., Hartmann, D. L., Grosvenor, D. P., McCoy, D. T., Hartmann, D. L., &

562   Grosvenor, D. P. (2014). Observed Southern Ocean Cloud Properties and Shortwave
563   Reflection. Part I: Calculation of SW Flux from Observed Cloud Properties*. *Journal of*
564   *Climate*, *27*(23), 8836–8857. https://doi.org/10.1175/JCLI-D-14-00287.1

565   Nazarenko, L., Rind, D., Tsigaridis, K., Del Genio, A. D., Kelley, M., & Tausnev, N. (2017).
566   Interactive nature of climate change and aerosol forcing. *Journal of Geophysical Research*,
567   *122*(6), 3457–3480. https://doi.org/10.1002/2016JD025809

568   Paluch, I. R. (1979). Entrainment Mechanism in Colorado Cumuli. *Journal of the Atmospheric*
569   *Sciences*, *36*(12), 2467–2478. https://doi.org/10.1175/1520-
570   0469(1979)036<2467:temicc>2.0.co;2

571   Petters, M. D., & Kreidenweis, S. M. (2007). A single parameter representation of hygroscopic
572   growth and cloud condensation nucleus activity. *Atmospheric Chemistry and Physics*, *13*(2),
573   1081–1091. https://doi.org/10.5194/acp-13-1081-2013

574   Qu, X., Hall, A., Klein, S. A., & Caldwell, P. M. (2015). The strength of the tropical inversion
575   and its response to climate change in 18 CMIP5 models. *Climate Dynamics*, *45*(1–2), 375–
576   396. https://doi.org/10.1007/s00382-014-2441-9

577   Raatikainen, T., Nenes, A., Seinfeld, J. H., Morales, R., Moore, R. H., Lathem, T. L., et al.
578   (2013). Worldwide data sets constrain the water vapor uptake coefficient in cloud
579   formation. *Proceedings of the National Academy of Sciences of the United States of*
580   *America*, *110*(10), 3760–3764. https://doi.org/10.1073/pnas.1219591110

581   Rauber, R. M., Stevens, B., Ochs, H. T., Knight, C., Albrecht, B. A., Blyth, A. M., et al. (2007).
582   Rain in Shallow Cumulus Over the Ocean: The RICO Campaign. *Bulletin of the American*
583   *Meteorological Society*, *88*(12), 1912–1928. https://doi.org/10.1175/BAMS-88-12-1912

584   Reutter, P., Su, H., Trentmann, J., Simmel, M., Rose, D., Gunthe, S. S., et al. (2009). Aerosol-
585   and updraft-limited regimes of cloud droplet formation: influence of particle number, size
586   and hygroscopicity on the activation of cloud condensation nuclei (CCN). *Atmospheric*
587   *Chemistry and Physics*, *9*(18), 7067–7080. Retrieved from %3CGo

588   Roberts, G. C., & Nenes, A. (2005). A continuous-flow streamwise thermal-gradient CCN

589   chamber for atmospheric measurements. *Aerosol Science and Technology*, *39*(3), 206–221.

590   https://doi.org/10.1080/027868290913988

591 Roberts, G. C., Ramana, M. V, Corrigan, C., Kim, D., & Ramanathan, V. (2008). Simultaneous

592   observations of aerosol-cloud-albedo interactions with three stacked unmanned aerial

593   vehicles. *Proceedings of the National Academy of Sciences of the United States of America*,

594   *105*(21), 7370–7375. https://doi.org/10.1073/pnas.0710308105

595 Rosenfeld, D., Zheng, Y., Hashimshoni, E., Pöhlker, M. L., Jefferson, A., Pöhlker, C., et al.

596   (2016). Satellite retrieval of cloud condensation nuclei concentrations by using clouds as

597   CCN chambers. *Proceedings of the National Academy of Sciences*, *113*(21), 5828–5834.

598   https://doi.org/10.1073/pnas.1514044113

599 Russell, L. M., & Seinfeld, J. H. (1998). Size- and Composition-Resolved Externally Mixed

600   Aerosol Model. *Aerosol Science and Technology*, *28*(5), 403–416.

601   https://doi.org/10.1080/02786829808965534

602 Russell, L. M., Lenschow, D. H., Laursen, K. K., Krummel, P. B., Siems, S. T., Bandy, A. R., et

603   al. (1998). Bidirectional mixing in an ACE 1 marine boundary layer overlain by a second

604   turbulent layer. *Journal of Geophysical Research Atmospheres*, *103*(D13), 16411–16432.

605   https://doi.org/10.1029/97JD03437

606 Russell, L. M., Seinfeld, J. H., Flagan, R. C., Ferek, R. J., Hegg, D. A., Hobbs, P. V., et al.

607   (1999). Aerosol dynamics in ship tracks. *Journal of Geophysical Research Atmospheres*,

608   *104*(D24), 31077–31095. https://doi.org/10.1029/1999JD900985

609 Sanchez, K. J., & Roberts, G. C. (2018). SOCRATES CCN measurements. Version 1.1.

610   UCAR/NCAR - Earth Observing Laboratory. https://doi.org/10.5065/D6Z036XB

611 Sanchez, K. J., Russell, L. M., Modini, R. L., Frossard, A. A., Ahlm, L., Corrigan, C. E., et al.

612   (2016). Meteorological and aerosol effects on marine cloud microphysical properties.

613   *Journal of Geophysical Research*, *121*(8), 4142–4161.

614   https://doi.org/10.1002/2015JD024595

615 Sanchez, K. J., Roberts, G. C., Calmer, R., Nicoll, K., Hashimshoni, E., Rosenfeld, D., et al.

616   (2017). Top-down and Bottom-up aerosol-cloud-closure: towards understanding sources of

617   uncertainty in deriving cloud radiative flux. *Atmospheric Chemistry and Physics*

618   *Discussions*, *17*(March), 1–32. https://doi.org/10.5194/acp-2017-201

619   Schnaiter, M., Järvinen, E., Abdelmonem, A., & Leisner, T. (2018). PHIPS-HALO: The airborne

620   particle habit imaging and polar scattering probe - Part 2: Characterization and first results.

621   *Atmospheric Measurement Techniques*, *11*(1), 341–357. https://doi.org/10.5194/amt-11-

622   341-2018

623   Seinfeld, J. H., & Pandis, S. N. (2006). *Atmospheric Chemistry and Physics: From Air Pollution*

624   *to Climate Change*. New York: Wiley. Retrieved from

625   https://books.google.com/books?id=tZEpAQAAMAAJ

626   Seinfeld, J. H., Bretherton, C. S., Carslaw, K. S., Coe, H., DeMott, P. J., Dunlea, E. J., et al.

627   (2016). Improving our fundamental understanding of the role of aerosol-cloud interactions

628   in the climate system. *Proceedings of the National Academy of Sciences of the United States*

629   *of America*, *113*(21), 5781–90. https://doi.org/10.1073/pnas.1514043113

630   Stephens, G. L. (1978). Radiation Profiles in Extended Water Clouds 2. Parameterization

631   Schemes. *Journal of the Atmospheric Sciences*, *35*(11), 2123–2132.

632   https://doi.org/10.1175/1520-0469(1978)035<2123:rpiewc>2.0.co;2

633   Stevens, B. (2002). Entrainment in stratocumulus-topped mixed layers. *Quarterly Journal of the*

634   *Royal Meteorological Society*, *128*(586 PART B), 2663–2690.

635   https://doi.org/10.1256/qj.01.202

636   Stevens, B. (2015). Rethinking the lower bound on aerosol radiative forcing. *Journal of Climate*,

637   *28*(12), 4794–4819. https://doi.org/10.1175/JCLI-D-14-00656.1

638   Stevens, B., Moeng, C. H., Ackerman, A. S., Bretherton, C. S., Chlond, A., de Roode, S., et al.

639   (2005). Evaluation of large-eddy simulations via observations of nocturnal marine

640   stratocumulus. *Monthly Weather Review*, *133*(6), 1443–1462.

641   https://doi.org/10.1175/MWR2930.1

642   de Szoeke, S. P., Fairall, C. W., Wolfe, D. E., Bariteau, L., & Zuidema, P. (2010). Surface flux

643   observations on the southeastern tropical pacific ocean and attribution of sst errors in

644   coupled ocean-atmosphere models. *Journal of Climate*, *23*(15), 4152–4174.

645   https://doi.org/10.1175/2010JCLI3411.1

646 Turton, J. D., & Nicholls, S. (1987). A Study of the Diurnal-Variation of Stratocumulus Using a

647   Multiple Mixed Layer Model. *Quarterly Journal of the Royal Meteorological Society*,

648   *113*(477), 969–1009. https://doi.org/10.1256/smsqj.47710

649 Twomey, S. (1977). The Influence of Pollution on the Shortwave Albedo of Clouds. *Journal of*

650   *the Atmospheric Sciences*, *34*(7), 1149–1152. https://doi.org/10.1175/1520-

651   0469(1977)034<1149:TIOPOT>2.0.CO;2

652 Tzivion, S., Feingold, G., & Levin, Z. (1987). An efficient numerical solution to the stochastic

653   collection equation. *Journal of the Atmospheric Sciences*, *44*(21), 3139–3149.

654   https://doi.org/10.1175/1520-0469(1987)044<3139:aenstt>2.0.co;2

655 UCAR/NCAR-Earth Observing Laboratory. (2018). NCAR HCR radar moments data. Version

656   1.0. UCAR/NCAR - Earth Observing Laboratory. https://doi.org/10.5065/D68914PH

657 UCAR/NCAR-Earth Observing Laboratory. (2019a). High Rate (HRT - 25 sps) Navigation,

658   State Parameter, and Microphysics Flight-Level Data. Version 1.0. UCAR/NCAR - Earth

659   Observing Laboratory. https://doi.org/.26023/K5VQ-K6KY-W610

660 UCAR/NCAR-Earth Observing Laboratory. (2019b). Low Rate (LRT - 1 sps) Navigation, State

661   Parameter, and Microphysics Flight-Level Data. Version 1.3. UCAR/NCAR - Earth

662   Observing Laboratory. https://doi.org/10.5065/D6M32TM9

663 Vial, J., Dufresne, J. L., & Bony, S. (2013). On the interpretation of inter-model spread in

664   CMIP5 climate sensitivity estimates. *Climate Dynamics*, *41*(11–12), 3339–3362.

665   https://doi.org/10.1007/s00382-013-1725-9

666 Wang, M., Ghan, S., Liu, X., L'Ecuyer, T. S., Zhang, K., Morrison, H., et al. (2012).

667   Constraining cloud lifetime effects of aerosols using A-Train satellite observations.

668   *Geophysical Research Letters*, *39*(15), 3–9. https://doi.org/10.1029/2012GL052204

669 Wang, S., Wang, Q., & Feingold, G. (2003). Turbulence, condensation, and liquid water

670   transport in numerically simulated nonprecipitating stratocumulus clouds. *Journal of the*

671   *Atmospheric Sciences*, *60*(2), 262–278. https://doi.org/10.1175/1520-

672   0469(2003)060<0262:TCALWT>2.0.CO;2

673 Webb, M. J., & Lock, A. P. (2013). Coupling between subtropical cloud feedback and the local

674   hydrological cycle in a climate model. *Climate Dynamics*, *41*(7–8), 1923–1939.

675   https://doi.org/10.1007/s00382-012-1608-5

676 Whittlestone, S., & Zahorowski, W. (1998). Baseline radon detectors for shipboard use:

677   Development and deployment in the First Aerosol Characterization Experiment (ACE 1).

678   *Journal of Geophysical Research-Atmospheres*, *103*(D13), 16743–16751.

679   https://doi.org/10.1029/98jd00687

680 Wood, R. (2007). Cancellation of Aerosol Indirect Effects in Marine Stratocumulus through

681   Cloud Thinning. *Journal of the Atmospheric Sciences*, *64*(7), 2657–2669.

682   https://doi.org/10.1175/JAS3942.1

683 Xue, H., & Feingold, G. (2006). Large-eddy simulations of trade wind cumuli: Investigation of

684   aerosol indirect effects. *Journal of the Atmospheric Sciences*, *63*(6), 1605–1622.

685   https://doi.org/10.1175/JAS3706.1

686 Yum, S. S., Hudson, J. G., & Xie, Y. (1998). *Comparisons of cloud microphysics with cloud*

687   *condensation nuclei spectra over the summertime Southern Ocean*. *Journal of Geophysical*

688   *Research Atmospheres* (Vol. 103). https://doi.org/10.1029/98JD01513

689 Zondlo, M. A., Paige, M. E., Massick, S. M., & Silver, J. A. (2010). Vertical cavity laser

690   hygrometer for the National Science Foundation Gulfstream-V aircraft. *Journal of*

691   *Geophysical Research Atmospheres*, *115*(20), 1–14. https://doi.org/10.1029/2010JD014445

692 Zuidema, P., Xue, H., & Feingold, G. (2008). Shortwave radiative impacts from aerosol effects

693   on marine shallow cumuli. *Journal of the Atmospheric Sciences*, *65*(6), 1979–1990.

694   https://doi.org/10.1175/2007JAS2447.1

695

696

697   **Figure 1**. The measurement derived q_v and θ_E for the RF12 (a) and RF10$_{Thick}$ (b) cases. The in-
698 cloud fit is the in-cloud q_v and θ_E calculated from linear fits of the temperature and pressure
699 vertical profiles with the assumption that in-cloud RH$_{liq}$ = 100%. The above cloud measurements
700 with red circles are the measurements that are used in the calculation to correct for the effect of
701 entrainment on the cloud microphysical and optical properties (See Supporting text S3 and S4 for
702 identifying entrained air properties and calculation details). The measurements marked as
703 entrained air are considered to be representative of the air properties that are entrained into the
704 cloud. The black solid and dashed lines are mixing lines connecting the cloud base properties to
705 three of the entrained air points and represent the expected total water content as a function of θ_E.
706 The mixing lines shown represent the median and 25th, 75th percentiles in LWC and CDNC
707 derived from all mixing lines and correspond to calculated LWC and CDNC profiles shown in
708 Figure 2. Similar plots for RF02, RF10$_{Thin}$ and RF13 are shown in Supporting Figure S4.

709   **Figure 2.** Observed and simulated cloud properties for the RF12 (a-d) and RF10$_{Thick}$ (e-h) case.
710 The observed properties were obtained from the CDP measurements, except for the extinction,
711 which was calculated from the observed CDP distributions. The ENT$_{LWC}$ and ENT$_{ML}$ D_v profile
712 is identical to the adiabatic profile due to the assumption of inhomogeneous entrainment. By
713 definition, the LWC for ENT$_{LWC}$ is the same as what was observed so there is no ENT$_{LWC}$ line
714 on the LWC profile. The ENT$_{ML}$ profile is dependent on the properties of the entrained air (red
715 circles in Figure 2). The solid black line is the median LWC and CDNC from the distribution of
716 profiles derived from the ENT$_{ML}$ analysis (Section 2.5) and the dashed lines represent the 25th
717 and 75th percentiles and correspond to the mixing lines shown in Figure 1. Vertical profiles for
718 RF02, RF10$_{Thin}$ and RF13 are shown in Supporting Figure S5.

719 **Table 1.** GV observed below-cloud aerosol concentrations, in-cloud droplet properties and
720 calculated optical properties. ACPM simulation results are present for adiabatic simulations, as
721 well as simulations for LWC entrainment method and mixing line entrainment method. The
722 sensitivity of below-cloud particle number concentration, updraft velocity and cloud LWP
723 (which is affected by cloud-top entrainment) on SWCF and CDNC. Sensitivities for SWCF are
724 calculated for both the adiabatic (ENT_{LWC}) simulations. Sensitivities for CDNC are the same for
725 adiabatic simulations and ENT_{LWC}.

	RF02	RF10$_{Thin}$	RF10$_{Thick}$	RF12	RF13
Observed					
$CDNC_{obs}$ (cm^{-3})	64±11	97±17	94±51	175±34	143±24
$SWCF_{obs}$ (W m^{-2})	103.1	142.9	340.1	234.3	201.1
Droplet spectra width[a]	0.81±0.04	0.84±0.03	0.73±0.12	0.82±0.05	0.83±0.05
Max LWC (g m^{-3})	0.23	0.30	0.68	0.40	0.36
LWP (g m^{-2})[b]	1.29	2.02	19.89	6.47	3.94
Below cloud Aerosol (cm^{-3})	457±9	463±62	956±17	505±52	290±66
Below cloud Aerosol (>70 nm, cm^{-3})	161±42	167±29	193±45	269±74	199±38
Cloud base height (m)	500	1010	290	1090	790
Cloud top height (m)	660	1210	870	1450	1030
Cloud base temperature (K)	274.9	273.3	283.9	268.3	274.3
Cloud top temperature (K)	273.9	272.1	281.1	265.7	272.6
Simulations					
			Adiabatic		
$CDNC_{adiabatic}$ (cm^{-3})	176	198	226	286	220
$SWCF_{adiabatic}$ (W m^{-2})[c]	196.5±17.1	220.8±16.5	387.3±9.4	272.7±8.9	242.2±7.0
Droplet spectra width	0.96	0.97	0.91	0.96	0.97
Max LWC (g m^{-3})	0.32	0.38	1.59	0.55	0.47
LWP (g m^{-2})	2.34	3.61	47.31	9.79	5.48
TOA incoming solar radiation (W m^{-2})	453.8	419.4	431.3	365.7	393.2
			LWC Entrainment (ENT_{LWC})		
$CDNC_{ENT_{LWC}}$ (cm^{-3})	97±24	109±40	115±60	188±18	156±21
$SWCF_{ENT_{LWC}}$ (W m^{-2})[c]	135.2±14.2	158.8±15.2	345.4±16.2	242.7±10.4	212.5±7.3
Entrainment reduction in adiabatic LWP	45%	44%	**58%**	34%	**28%**
SWCF for **28%** and **58%** reduction from adiabatic LWP (W m^{-2})	161.0, 110.2	186.4, 133.5	372.6, 339.6	248.1, 201.8	210.7, 158.3
			Mixing Line Entrainment (ENT_{ML}; Sanchez et al. 2017)[d]		
$CDNC_{ENT_{ML}}$ (cm^{-3}) 50th percentile	79±10	160±5	166±65	151±20	132±19
25th and 75th percentiles	17.7-103	127-176	161-172	134-191	109-220
$SWCF_{ENT_{ML}}$ (W m^{-2}) 50th percentile	102.2±12.1	197.1±16.2	367.7±12.8	220.5±11.0	189.3±7.6
25th and 75th percentiles	27.2-128.6	172.9-207.9	365.4-370.6	220.5-241.1	170.7-242.2
			Difference between simulated and observed SWCF[c]		
$\delta SWCF_{adiabatic}$	93.4±17.1	77.9±16.5	47.2±9.4	38.4±8.9	41.1±7.0
$\delta SWCF_{ENT_{LWC}}$	32.1±14.2	15.9±15.2	5.3±16.2	8.4±10.4	11.4±7.3
$\delta SWCF_{ENT_{ML}}$	-0.9±12.1	54.2±16.2	27.6±12.8	-13.8±11.0	-11.8±7.6
Sensitivity Tests			$S(X_i) = dln(Y_i)/dln(X_i)$ (Feingold et al., 2003)		
X_i			**Y_i = SWCF**		
N_p	0.149 (0.145)	0.109 (0.130)	0.031 (0.059)	0.060 (0.088)	0.084 (0.090)
w	0.033 (0.034)	0.027 (0.042)	0.014 (0.027)	0.022 (0.033)	0.019 (0.021)
LWP	0.632	0.569	0.132	0.281	0.397
X_i			**Y_i = $CDNC_{avg}$**		
N_p	0.776	0.707	0.888	0.743	0.705
w	0.433	0.428	0.485	0.301	0.250
LWP	1.014	1.025	0.776	1.007	1.053

726 [a](Martin et al., 1994). [b]Liquid water path is calculated from CDP distribution profile. [c]The uncertainty includes the potential error
727 of ± 20 % in updraft velocity (*w*) and the standard error of the CCN concentration measurements. [d]The 25th, 50th and 75th
728 percentile in SWCF and CDNC obtained from the distribution of profiles generated by the ENT_{ML} analysis (Section 2.5, Figure
729 1,2).

Figure1.

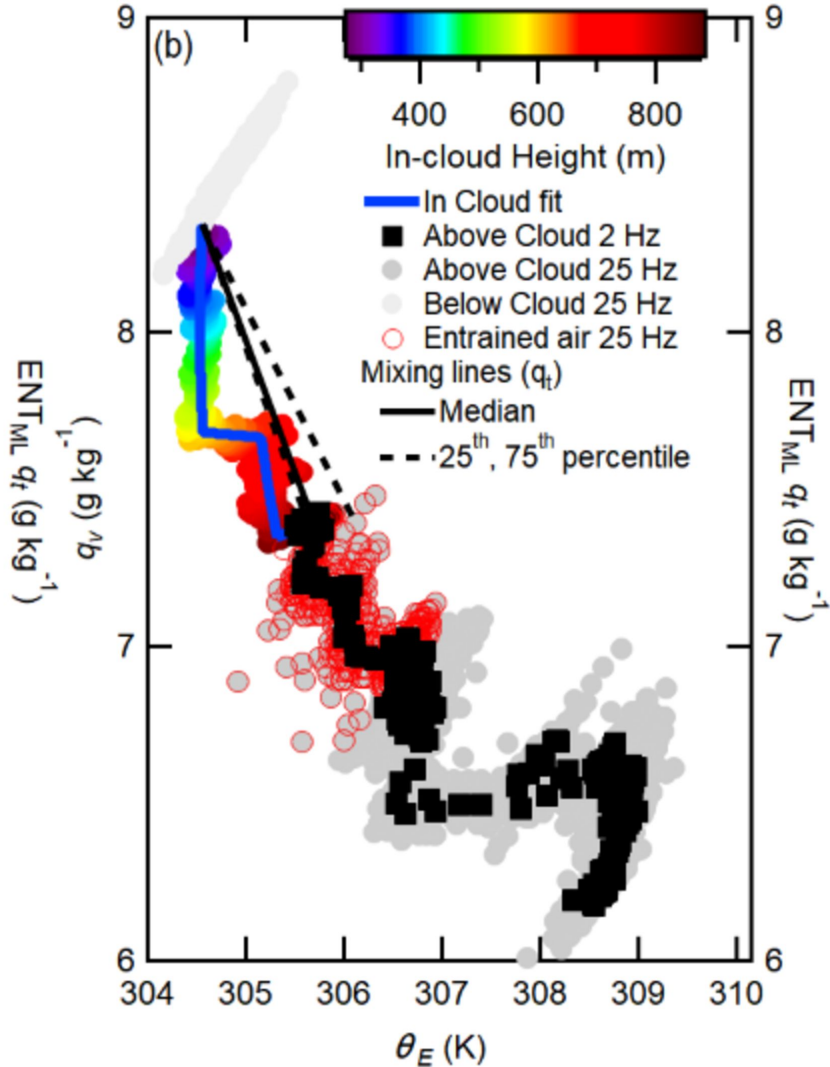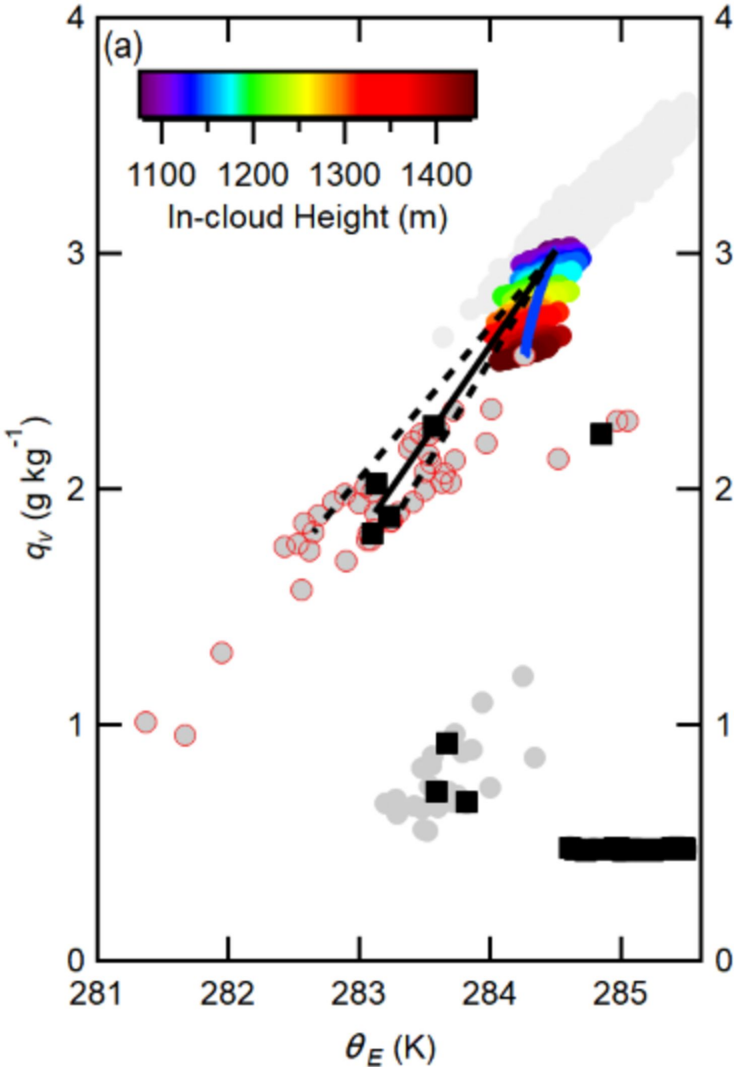(a) In-cloud Height (m): 1100, 1200, 1300, 1400

(b) In-cloud Height (m): 400, 600, 800
- In Cloud fit
- Above Cloud 2 Hz
- Above Cloud 25 Hz
- Below Cloud 25 Hz
- Entrained air 25 Hz
- Mixing lines (q_t)
  - Median
  - 25th, 75th percentile

Figure2.

Legend: ● Observed — Adiabatic — ENT_{ML} — ENT_{LWC}

Plots arranged in two rows (RF12 and RF10$_{Thick}$) and four columns.

Left axes:
- RF12: Height (m), ranging 1000 to 1500
- RF10$_{Thick}$: Height (m), ranging 200 to 900

Bottom axes (x):
- D_V (μm): 0, 10, 20
- LWC (g kg^{-1}): 0.0, 0.2, 0.4, 0.6, 0.8, 1.0 (with 300)
- CDNC (cm^{-3}): 0, 100, 200, 300
- Extinction (km^{-1}): 0, 40, 80, 120

Panel labels: (a), (b), (c), (d) top row; (e), (f), (g), (h) bottom row.